



Rational construction of “all-in-one” metal-organic framework for integrated solar steam generation and advanced oxidation process

Panpan He^a, Hongyu Lan^b, Huiying Bai^a, Yingying Zhu^b, Zifen Fan^a, Jie Liu^a, Lijie Liu^a, Ran Niu^a, Zhiyue Dong^{b,*}, Jiang Gong^{a,c,**}

^a Key Laboratory of Material Chemistry for Energy Conversion and Storage, Ministry of Education, Hubei Key Laboratory of Material Chemistry and Service Failure, Semiconductor Chemistry Center, Hubei Engineering Research Center for Biomaterials and Medical Protective Materials, School of Chemistry and Chemical Engineering, Huazhong University of Science and Technology, Wuhan 430074, China

^b Collaborative Innovation Center for Advanced Organic Chemical Materials Co-constructed by the Province and Ministry, Ministry of Education Key Laboratory for the Synthesis and Application of Organic Functional Molecules and College of Chemistry and Chemical Engineering, Hubei University, Wuhan 430062, China

^c Key Laboratory of Polymer Processing Engineering (South China University of Technology), Ministry of Education, Guangzhou 510641, China



ARTICLE INFO

Keywords:

Solar energy
Interfacial solar steam generation
Advanced oxidation process
Peroxymonosulfate
Metal-organic framework

ABSTRACT

Integrating interfacial solar steam generation with advanced oxidation process (AOP) is regarded as a promising strategy for addressing energy and environmental issues. However, developing dual-functional evaporators well-integrated with synergistic photothermal-AOP catalysis properties remains challenging. Herein, we synthesize cobalt-based metal-organic framework (Co-CAT) and prepare dual-functional Co-CAT evaporators. Co-CAT is endowed with “all-in-one” functions, i.e., high specific surface area, effective light absorption, and high catalytic activity. Co-CAT exhibits superior sunlight absorption and photo-to-thermal conversion property. The large specific surface area and abundant micropore of Co-CAT facilitate water permeation and evaporation enthalpy reduction. COMSOL Multiphysics and density functional theory calculation results prove that Co^{2+} sites in Co-CAT and heat localization promote peroxymonosulfate activation. Consequently, it not only exhibits a high-water evaporation rate of $2.2 \text{ kg m}^{-2} \text{ h}^{-1}$, outperforming the-state-of-art evaporators, but also presents the notable tetracycline degradation efficiency (91.1%). This work proposes an ingenious way to deal with freshwater shortage and water pollution.

1. Introduction

Global freshwater scarcity and energy crisis have become ever severe for the persistent population growth, rapid urbanization, and serious water pollution [1–4]. Employing non-portable wastewater or seawater to produce freshwater is an essential way to meet the enormous demand for freshwater [5]. Conventional water treatment technologies such as reverse osmosis and membrane distillation are plagued by high equipment investment and fossil energy consumption [6]. Solar energy is a clean, free, and inexhaustible source, and has been widely exploited for generating electricity, thermal, fuels, and so forth [7–12]. The effective utilization of solar energy is believed as the ultimate answer to address energy and environmental issues in the future. Recently, interfacial solar

steam generation (ISSG), which confines photothermal materials to the air-water interface, is taken for an eco-friendly and economical technology by utilizing renewable solar energy [13–18]. In comparison to conventional bottom or bulk heating configuration, ISSG reduces heat diffusion into bulk water and achieves high energy conversion efficiency [19–23]. Nevertheless, if the water source has already been polluted by non-biodegradable and noxious organic compounds such as pharmaceuticals, those organic pollutants may evaporate along with water vapor to contaminate the condensed water and even get concentrated in the water source after evaporation, leading to secondary pollution [24].

To tackle with this problem, great effort has been made to the integration of ISSG with water de-contamination technology [25–27]. Advanced oxidation process (AOP) is an important method for the

* Corresponding author.

** Corresponding author at: Key Laboratory of Material Chemistry for Energy Conversion and Storage, Ministry of Education, Hubei Key Laboratory of Material Chemistry and Service Failure, Semiconductor Chemistry Center, Hubei Engineering Research Center for Biomaterials and Medical Protective Materials, School of Chemistry and Chemical Engineering, Huazhong University of Science and Technology, Wuhan 430074, China.

E-mail addresses: dzyue@hubu.edu.cn (Z. Dong), gongjiang@hust.edu.cn (J. Gong).

degradation of organic pollutants by producing reactive oxygen species (ROS), including photocatalysis, Fenton oxidation, persulfate oxidation, and so on [28–30]. The combination of ISSG and photocatalysis has aroused huge research interest in recent years, in which photothermal materials usually absorb long-wave photon for photothermal evaporation, while semiconductor photocatalysts generally absorb short-wave photon for photocatalytic degradation of pollutants [31]. However, photothermal materials and photocatalysts are normally two separate modules that need to be isolated and operated separately. Such integration system often suffers from complex designs and/or preparation processes and hinders the integrated use of solar energy, owing to the small penetration depth of light. The other emerging tactic is the marriage of ISSG with sulfate radical-based AOP (SR-AOP). With the merits of long half-life, high redox potential, and high selectivity, SR-AOP has drawn widespread attention for constructing synergistic photothermal-catalytic system. In the integration design of ISSG and SR-AOP, the combination of localized heat arisen from photothermal materials and the active sites of catalysts synergistically accelerate the activation of persulfate such as peroxymonosulfate (PMS, HSO_5^-) to generate ROS for the degradation of pollutants [32–37]. For example, Yin et al. fabricated a Co_3S_4 nanoparticle/polyacrylonitrile bilayer membrane, in which Co_3S_4 exhibited photothermal effect and PMS activation ability jointly, and polyacrylonitrile fiber served as a hydrophilic and adiabatic substrate for water transport and heat localization [38]. However, since AOP catalysts and photothermal materials usually display different thermal conductivity, the localized solar heat arisen from photothermal materials could not be promptly transferred to catalysts; thereby, the activation efficiency of persulfate is not satisfactory. Additionally, previous SR-AOP catalysts often own low specific surface areas, so many active sites are not readily available for persulfate activation. In this context, developing all-in-one, dual-functional evaporator well-integrated with highly porous structure, exposed active site, and photothermal-catalytic property is at the core of the problem, but remains a great challenge.

Metal-organic frameworks (MOFs), a class of crystalline materials composed of metal ions/clusters and ligands, are characterized by high specific surface areas, adjustable apertures, and designable

compositions [39–41]. Over the last three decades, MOFs have been vastly employed for heterogeneous catalysis [42], gas storage and separation [43], sensing [44], energy storage and conversion [45–47], etc. Especially, cobalt-based MOFs are proved as efficient SR-AOP catalysts, in which uniformly distributed cobalt ions act as catalytic sites for PMS activation [48]. Thereby, the rational design of MOFs with “all-in-one” functions, i.e., high specific surface areas, superior photothermal conversion, and abundant SR-AOP catalytic sites for realizing the effective synergy of ISSG and AOP provides a promising platform towards simultaneous freshwater production and pollutant remediation, which however as far as we know has not been touched. In this contribution, we initially prepare a cobalt-based MOF (namely Co-CAT) via a simple hydrothermal method and fabricate a Co-CAT evaporator by dip-coating Co-CAT particles on the cotton cloth for integrating interfacial solar evaporation with AOP-induced tetracycline (TC) degradation (Fig. 1). The Co-CAT shows large specific surface area ($418 \text{ m}^2 \text{ g}^{-1}$) and uniform micro-aperture (1.4 nm), which are available for high sunlight absorption (ca. 97 %), thermal conversion, and reduction of vaporization enthalpy. The Co^{2+} of Co-CAT serves as the highly dispersed catalytic site for PMS activation. Thanks to the above merits, Co-CAT evaporator shows high water evaporation rate ($2.2 \text{ kg m}^{-2} \text{ h}^{-1}$) and efficient degradation of TC (91.1 %) under 1 Sun irradiation, demonstrating the synergy of photothermal conversion and SR-AOP catalysis.

2. Experimental section

2.1. Reagents and materials

2,3,6,7,10,11-Hexahydroxytriphenylene ($\text{C}_{18}\text{H}_{12}\text{O}_6$, HHTP), cobalt acetate tetrahydrate ($\text{C}_4\text{H}_{14}\text{CoO}_8$, $\text{Co}(\text{OAc})_2 \cdot 4\text{H}_2\text{O}$), and 1-methyl-2-pyrrolidone ($\text{C}_5\text{H}_9\text{NO}$, NMP) were purchased from Adamas Reagent Co. Ltd. Acetone, methanol, formic acid, ethanol, and *tert*-butanol were obtained from Sinopharm Chemical Reagent Co. Ltd. Tetracycline ($\text{C}_{22}\text{H}_{24}\text{N}_2\text{O}_8$, TC) was supplied by Macklin. Peroxymonosulfate ($\text{KHSO}_5 \cdot 0.5\text{KHSO}_4 \cdot 0.5\text{K}_2\text{SO}_4$, PMS) and 2,2,6,6-tetramethylpiperidine (TEMP) were supported by Aladdin. *p*-Benzoquinone and 5,5-dimethyl-1-pyrroline-oxide (DMPO) were obtained from InnoChem.

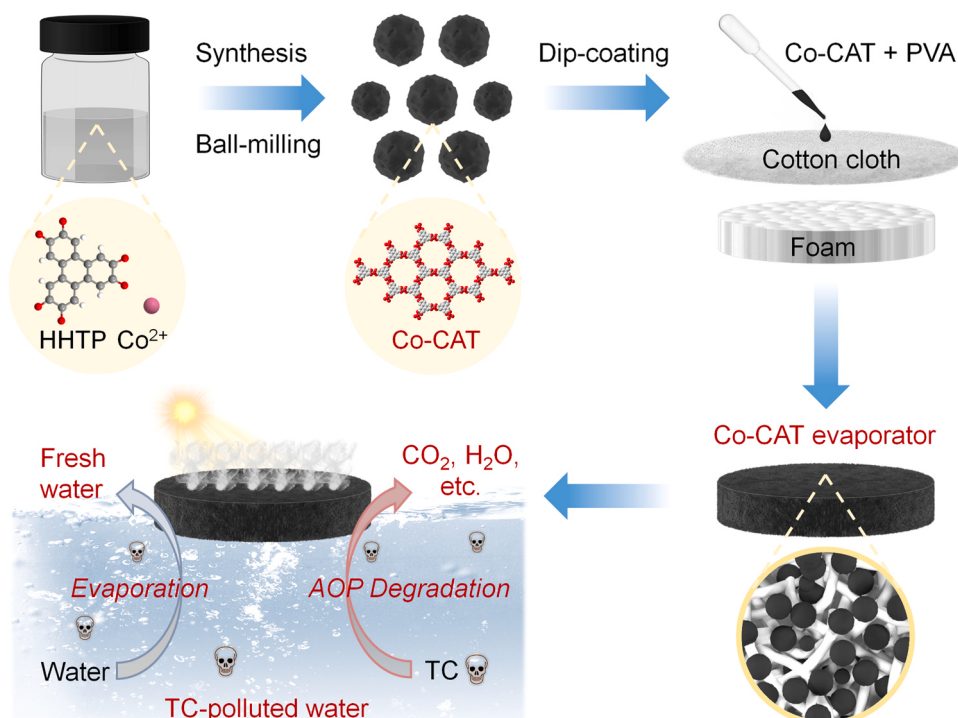


Fig. 1. Scheme for the construction of the Co-CAT evaporator for simultaneous interfacial water evaporation and TC degradation.

Poly(vinyl alcohol) (PVA, $M_w = 80,000\text{--}90,000 \text{ g mol}^{-1}$) and L-histidine were supplied by Kuraray and REGAL, respectively. Cotton cloth was supplied by EAXAY.

2.2. Preparation of Co-CAT evaporator

As depicted in Fig. 1, Co-CAT was synthesized by the hydrothermal method of HHTP and $\text{Co(OAc)}_2 \cdot 4 \text{ H}_2\text{O}$ based on the literature with some modifications [49]. Primarily, HHTP (0.700 g) and $\text{Co(OAc)}_2 \cdot 4 \text{ H}_2\text{O}$ (1.000 g) were added to 150 mL deionized water in a glass vial, which was sonicated for 30 min until the solid was dissolved. 16.5 mL NMP was dropwise added to the above solution, and then vigorously stirred to form a dark solution. Afterwards, the mixture was heated in the isothermal oven at 85 °C for 24 h to form Co-CAT crystal, which was washed 3 times with deionized water for 3 days, refreshed 6 times with acetone for 3 days, and vacuum dried at 85 °C for 24 h. The as-synthesized Co-CAT crystal was ball milled at 20 Hz for 60 min by vibrational ball mill (MSK-SFM-LN-192) to obtain fine powder (Note: After ball milling, the size of Co-CAT decreases greatly, which favors for the dispersion of Co-CAT particles in PVA solution and the uniform coating of Co-CAT on the surface of cotton cloth). Afterwards, 5 mg of PVA was added to 1 mL hot water to obtain a sticky PVA solution, and then Co-CAT powder with an optimized dosage (50 mg) was uniformly dispersed in PVA solution by stirring. Subsequently, the above mixture was dip-coated on a cotton cloth with a diameter of 4.8 cm, which was supported by a polystyrene (PS) foam with a diameter of 3.8 cm and a thickness of 0.5 cm, and dried at room temperature to acquire Co-CAT evaporator (Fig. S1).

2.3. Characterization

Scanning electron microscope (SEM, SU8010) and energy dispersive X-ray spectrometer (EDS) were utilized to reveal the morphology and element distribution, respectively. High-resolution transmission electron microscope (HRTEM, Tecnai F20) was used to investigate the microstructure. Surface area analyzer (Micromeritics ASAP 2460) was conducted to study the pore structure, and the pre-heating temperature and time of sample were 85 °C and 24 h, respectively. Pore size distribution was determined on density functional theory (DFT) model. Solid-state ^{13}C nuclear magnetic resonance (NMR) using Bruker 400 M spectrometer was employed to analyze the chemical structure. X-ray diffraction (XRD) using SmartLab-SE diffractometer was used to reveal the crystal structure. Water contact angle was recorded by micro optical contact angle measurement instrument (Dataphysics OCA15EC). The mechanical strength of sample was measured by tensile testing machine, and the stretching rate was 10 mm min⁻¹. Sunlight absorption property was estimated by UV-Vis-NIR spectrophotometer (Lambda 750 S). Thermal conductivity was tested by thermal conductivity analyzer (Hot Disk, TPS 2500). The evaporation behavior was monitored by differential scanning calorimeter (DSC, DSC2500). Electron paramagnetic resonance (EPR) using EMXmicro-6/1 spectrometer was employed to identify ROS. Degradation intermediates were revealed by ultra-performance liquid chromatography-mass spectrometer (UPLC-MS, Ultimate 3000 UHPLC-Q Exactive). Total organic carbon (TOC) was detected by TOC analyzer (Shimadzu, TOC-L).

2.4. Solar steam generation by Co-CAT evaporator

The evaporation device (Fig. S2) is composed of an electronic balance (JA2003) and a solar light simulator (CEL-S500L). The ambient temperature and relative humidity were ca. 36 °C and 32 %, respectively. The surface temperature of evaporator was monitored by infrared camera (DMI220). Water evaporation rate ($m, \text{kg m}^{-2} \text{ h}^{-1}$) and solar-to-vapor conversion efficiency ($\eta, \%$) were calculated by below equations,

$$m = \Delta m / (S \times t) \quad (1)$$

$$\eta = m' \times h_{\text{LV}} / (3600 \times P_{\text{in}}) \quad (2)$$

where Δm represents water mass loss in 1 h (kg), S refers to illuminated area of evaporator ($1.134 \times 10^{-3} \text{ m}^2$), t stands for irradiation time (1 h), m' stands for evaporation rate that subtracts dark evaporation rate ($0.22 \text{ kg m}^{-2} \text{ h}^{-1}$), h_{LV} is enthalpy of vaporization (kJ kg^{-1}), and P_{in} is illumination intensity (1 kW m^{-2} , i.e., 1 Sun).

2.5. Catalytic degradation of TC by Co-CAT evaporator

TC, a common antibiotic for the treatment of human and animal infections, has been frequently detected in water in recent years, which poses a serious threat to ecological security. In our experiment, TC degradation was conducted in a beaker with TC solution (50 ppm, 75 mL) and Co-CAT evaporator. The beaker was firstly placed in the darkness for 30 min, during which 1 mL solution was extracted and analyzed by high performance liquid chromatograph (HPLC, WUFENG LC-P100) every 15 min. Afterwards, PMS was added to the solution (0.07 g L⁻¹) and exposed to the illumination (1 kW m^{-2}) for 60 min, during which 1 mL solution was extracted and analyzed by HPLC every 10 min. The TC degradation efficiency was equal to the peak area ratio of degraded solution to original solution at the retention time of ca. 5.56 min and UV absorption wavelength of 355 nm, with mobile phase (methanol/0.2 wt% formic acid solution = 30/70 v/v, 1.0 mL min⁻¹).

3. Results and discussion

3.1. Preparation and characterization of Co-CAT

Co-CAT crystal was prepared by reacting HHTP ($\text{C}_{18}\text{H}_{12}\text{O}_6$) with cobalt (II) acetate in aqueous solution (Fig. 2a). After washing and drying, the as-synthesized Co-CAT crystal was milled to fine powder. As shown in Figs. 2b and 2c, for the crystal structure, Co-CAT belongs to the trigonal space group, which consists of two types of layers. One layer exhibits a honeycomb-like structure, in which each Co atom is combined with two deprotonated HHTP and two H_2O to form Co-O_6 octahedral coordination and result in the formation of $\text{Co}_3(\text{HHTP})_2(\text{H}_2\text{O})_6$ layer (Fig. 2d). The other layer is composed of discrete units, where each Co atom is coordinated to one HHTP and four H_2O to form octahedron and generate $\text{Co}_3(\text{HHTP})(\text{H}_2\text{O})_{12}$ (Fig. 2e). The axial H_2O in discrete units and HHTP in honeycomb layer are hydrogen-bonded, forming the integrated layers.

The morphology and microstructure of the as-prepared Co-CAT were characterized by SEM and HRTEM. Co-CAT presents as the black powder with irregular particle morphology (Figs. 3a and S3a), which results from the milling procedure. HRTEM image (Fig. 3b) exhibits the lattice fringe with a spacing of 1.68 nm, ascribed to (100) plane of Co-CAT. Besides, according to the N_2 adsorption-desorption isothermal curves, Co-CAT possesses a large BET specific surface area ($418 \text{ m}^2 \text{ g}^{-1}$) with abundant micropores (Fig. 3c). The DFT pore size distribution curve demonstrates that the aperture in Co-CAT is centered on 1.4 nm, close to the theoretical value of 1.2 nm, and a small portion of mesopore size is located at 2.4 and 4.4 nm (Fig. 3d). Evidently, high specific surface area is available for light trapping and mass transfer, and abundant micropores favor the reduction of vaporization enthalpy [50]. Moreover, in solid-state ^{13}C NMR spectrum, the chemical shifts at 109, 127 and 144 ppm are ascribed to three kinds of carbon atoms of HHTP in different chemical environment (Fig. 3e). Additionally, the as-prepared Co-CAT exhibits a comparable XRD pattern with the simulated one, confirming the proper crystal structure of Co-CAT in this work (Fig. 3f).

3.2. Characterization of Co-CAT evaporator

As shown in Fig. 4a, the Co-CAT evaporator was facilely prepared by dispersing Co-CAT powder in PVA solution, followed by dip-coating Co-CAT suspension on cotton cloth supported by PS foam, in which PVA

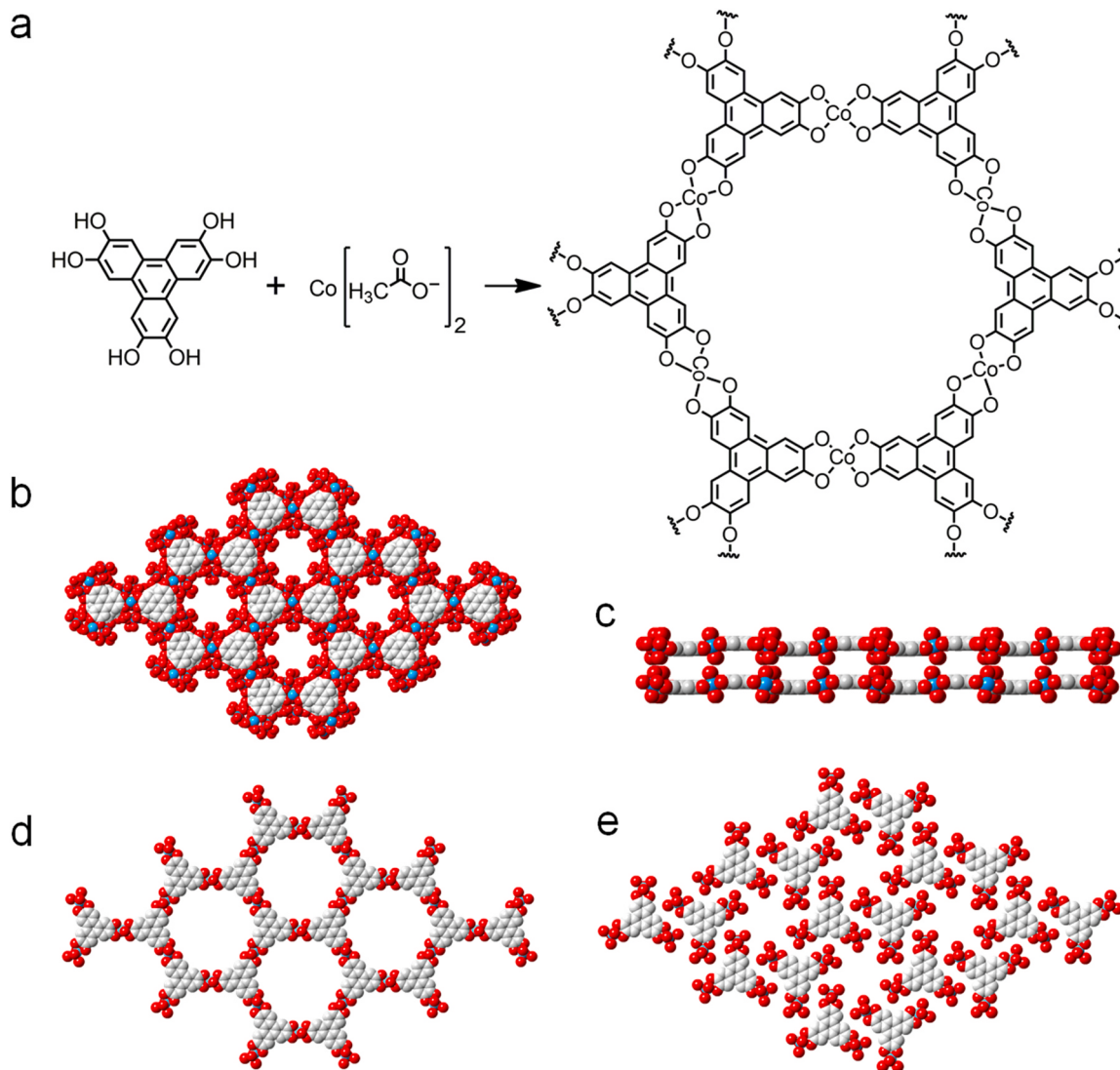


Fig. 2. (a) Scheme of synthesizing Co-CAT. (b and c) Schemes for crystal structure of Co-CAT from different views. (d and e) Schemes for the two types of layers in Co-CAT. Color code: C, gray; O, red; Co, blue. H is omitted for clarity.

functions as the binder for Co-CAT particles and cotton fibers. A large-size Co-CAT membrane with an area of ca. 400 cm^2 was readily fabricated, illustrating the scalability of Co-CAT evaporator (Fig. 4b). Based on SEM analysis, Co-CAT particles are well combined with cotton cloth by covering the surface or filling the interspace of cotton fibers with the help of PVA (Fig. 4b and S3b–S3d), which ensures sufficient light absorption and fast water permeation. EDS mapping images display that C, O and Co elements are uniformly distributed in the membrane (Fig. 4d–f), which facilitate the exposure of catalytic sites. Water contact angle measurement was employed to investigate the wettability of evaporator. The water contact angle quickly turns to 0° within 0.04 s for cotton cloth (Fig. S4a, Video S1), indicating the great hydrophilicity of cotton cloth for the cellulose component. Co-CAT evaporator gets fully wetted within 0.12 s (Fig. 4g, Video S2), illustrating that Co-CAT evaporator exhibits desirable wettability, which is related with the porous structure of Co-CAT. Overtly, the favorable hydrophilic property of Co-CAT evaporator is conducive to the fast water transport for interfacial solar evaporation [51,52]. Moreover, the tensile measurement (Fig. 4h) and load-carrying experiment (Fig. 4i) indicate the satisfying mechanical strength of Co-CAT membrane, and the deformation experiment (Fig. 4j) illustrates the good flexibility of Co-CAT membrane.

Supplementary material related to this article can be found online at doi:10.1016/j.apcatb.2023.123001.

3.3. Optical absorption and thermal conversion properties of Co-CAT evaporator

Sunlight absorption and solar-to-thermal conversion properties are essential for photothermal materials [53–55]. Primarily, the sunlight absorptivity was investigated. As Fig. 5a shows, Co-CAT evaporator exhibits a broadband light absorption (300–2500 nm) with high absorptivity (97–98 %), overtly surpassing that of cotton cloth (44–62 %). In addition, as Fig. 5b displays, the surface temperature of Co-CAT evaporator grows from 35.8°C to 104.6°C within 2 min under 1 Sun illumination, obviously quicker than that of cotton cloth (from 37.3°C to 44.8°C). The temperature of Co-CAT evaporator maintains at 106.6°C as illumination time increases to 10 min, while it rapidly decreases to 35.9°C within 4 min with light off, stating the remarkable photothermal conversion capacity of Co-CAT. As a supplement, infrared images of cotton cloth and Co-CAT evaporator are provided in Figs. 5c and 5d, respectively.

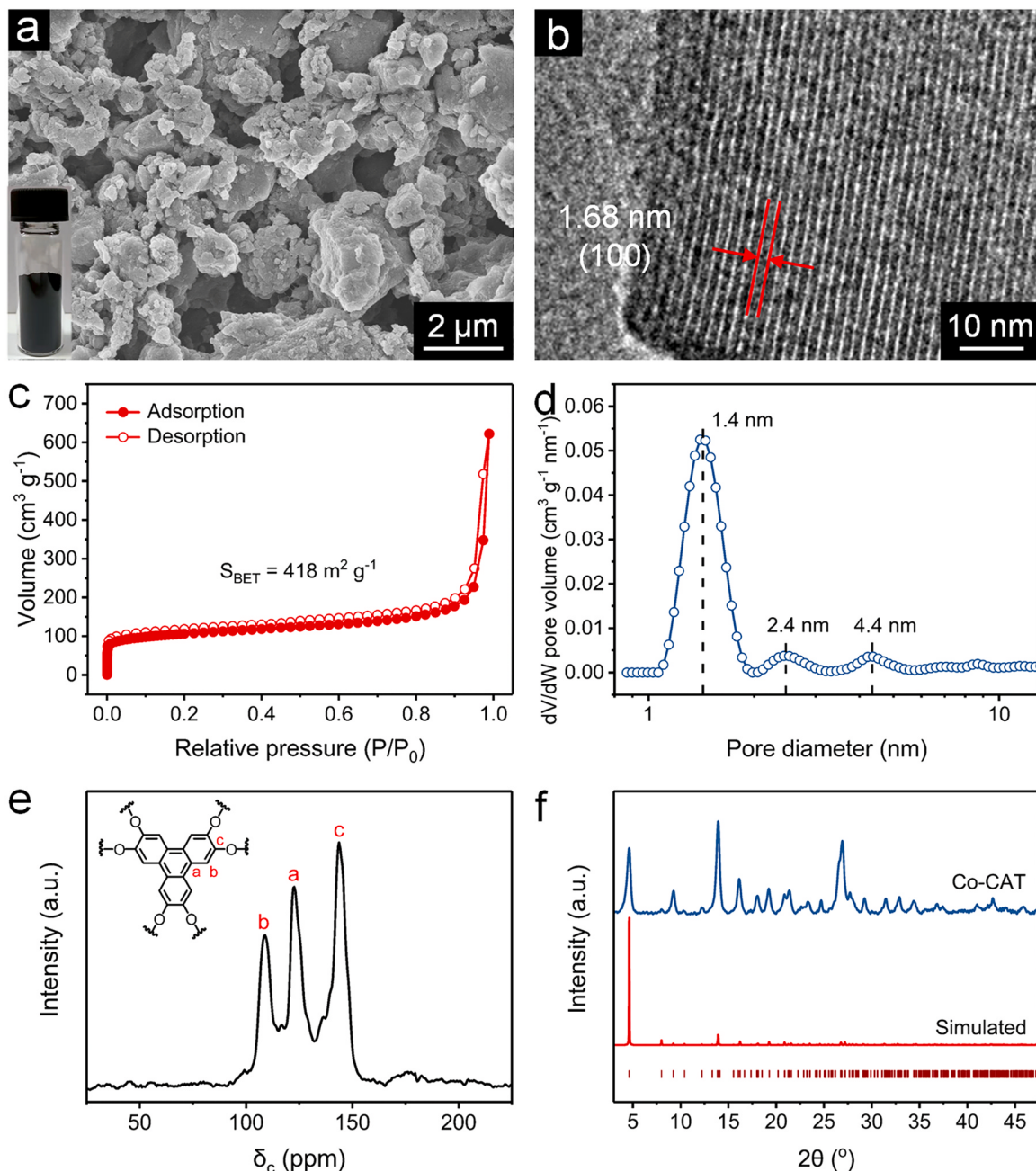


Fig. 3. (a) SEM image and photograph of Co-CAT, (b) HRTEM image, (c) nitrogen adsorption-desorption isothermal curves, (d) DFT aperture distribution curve, (e) solid-state ^{13}C NMR spectrum, and (f) XRD pattern of Co-CAT.

3.4. Interfacial solar steam generation of Co-CAT evaporator

The water evaporation was performed on a lab-made system consisting of electronic balance and solar light simulator (Figs. 6a and S2). TC solution (50 ppm, 75 mL) was used as polluted-water source, and the evaporator floats on the TC solution. As exhibited in Fig. 6b, the water mass loss is linearly related with time under 1 Sun illumination. Accordingly, the evaporation rate of TC solution (Blank, $0.65 \text{ kg m}^{-2} \text{ h}^{-1}$) or using cotton cloth (Cotton, $0.78 \text{ kg m}^{-2} \text{ h}^{-1}$) is obviously lower than that using Co-CAT evaporator (Co-CAT, $2.13 \text{ kg m}^{-2} \text{ h}^{-1}$) or further adding PMS (Co-CAT + PMS, $2.17 \text{ kg m}^{-2} \text{ h}^{-1}$) (Fig. 6c). In fact, the surface temperature of Co-CAT evaporator in wet condition (ca. 56°C) obviously exceeds that of cotton cloth (ca. 42°C , Fig. 6d), ascribed to the superior photothermal conversion by Co-CAT, which is conductive to the effective interfacial heating and fast water

evaporation. Supportably, infrared images of Co-CAT evaporator in wet condition are provided in Fig. S5.

The effect of the Co-CAT dosage on the evaporation performance was investigated. As shown in Fig. S6a, as the Co-CAT dosage grows from 0 mg to 75 mg, the evaporator exhibits an increased surface coverage of Co-CAT. As displayed in Fig. S6b and S6c, when the Co-CAT dosage increases from 0 mg to 50 mg, the evaporation rate rises from $0.78 \text{ kg m}^{-2} \text{ h}^{-1}$ (for 0 mg) to $1.86 \text{ kg m}^{-2} \text{ h}^{-1}$ (for 25 mg) and $2.17 \text{ kg m}^{-2} \text{ h}^{-1}$ (for 50 mg). When the Co-CAT dosage ascends to 75 mg, the evaporation rate mildly increases to $2.25 \text{ kg m}^{-2} \text{ h}^{-1}$, illustrating that overmuch Co-CAT would not obviously enhance the evaporation rate, since the light absorption has reached saturation. Besides, the influence of PMS or TC concentration on evaporation property was studied. The water evaporation rate using Co-CAT evaporator keeps at around $2.15 \text{ kg m}^{-2} \text{ h}^{-1}$, when the TC concentration ranges from

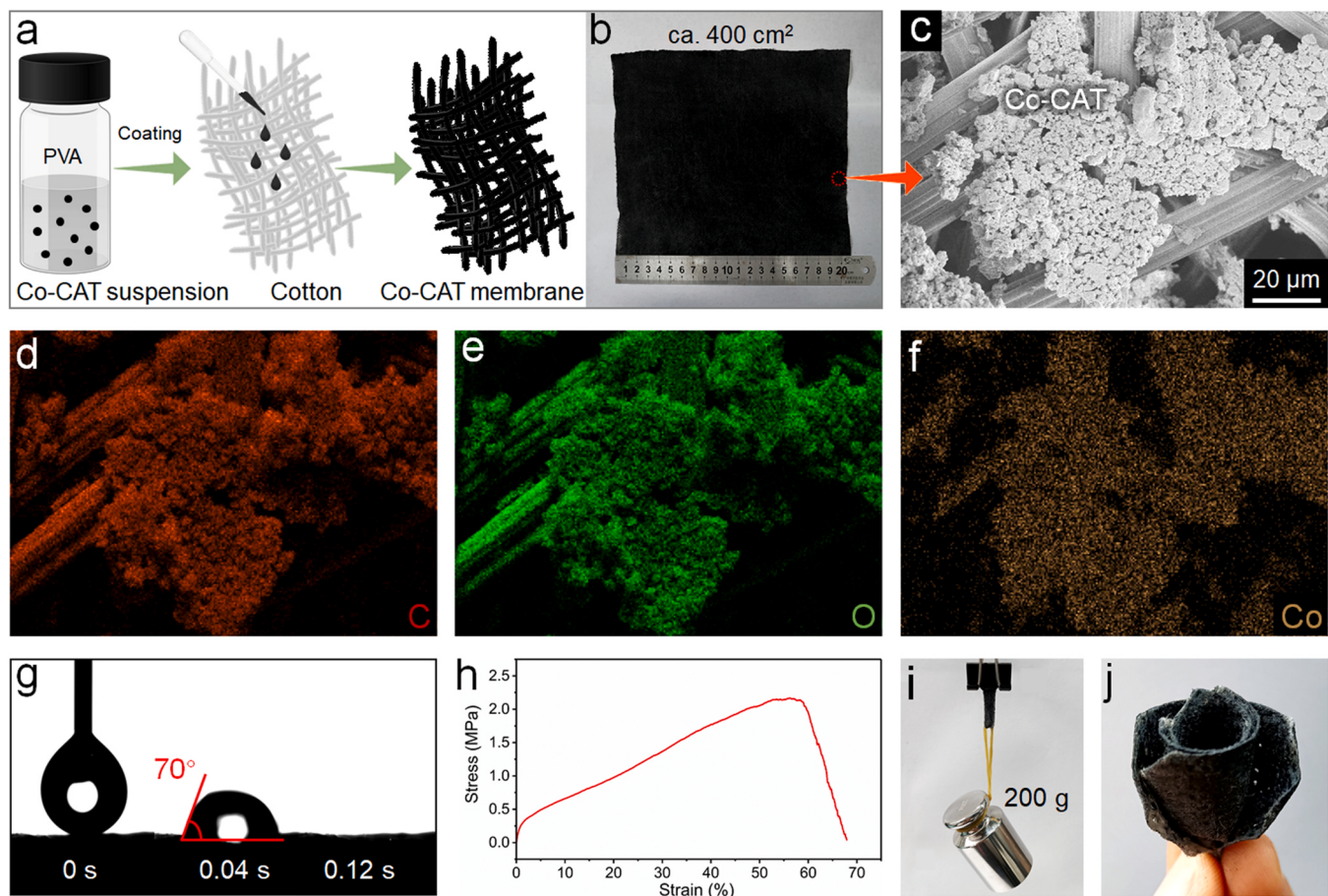


Fig. 4. (a) Scheme of synthesizing Co-CAT evaporator. (b) Photograph of a large-size Co-CAT membrane. (c) SEM image and (d–f) EDS mapping images of Co-CAT membrane. (g) Time evolution of the water contact angle. (h) Stress-strain stretching curve of Co-CAT membrane. Photographs of (i) load-carrying or (j) folded Co-CAT membrane.

25 ppm to 100 ppm (Fig. S7a) or the PMS concentration changes from 0.03 g L⁻¹ to 0.09 g L⁻¹ (Fig. S7b), indicating the ignorable impacts of TC and PMS concentrations on the evaporation property. Furthermore, the evaporation performance of Co-CAT evaporator under different irradiation intensities was studied (Fig. S8). When the irradiation intensity increases from 0.5 Sun to 2.5 Sun, the evaporation rate rises from 1.27 kg m⁻² h⁻¹ to 5.06 kg m⁻² h⁻¹.

Additionally, interfacial solar evaporation was conducted for 20 cycles to test the recyclability of Co-CAT evaporator. As shown in Fig. 6e, the water evaporation rate keeps above 2.1 kg m⁻² h⁻¹, demonstrating the notable recycling stability of Co-CAT evaporator. Besides, the Co-CAT evaporator maintains the good appearance stability after 3 cycles (Fig. S9), proving its good recyclability in the presence of PMS and TC. Indeed, Co-CAT evaporator exhibits prominent performance compared with previous work (Fig. 6f and Table S1), such as TiO₂/nickel foam (1.25 kg m⁻² h⁻¹) [56], 3D graphene network (1.64 kg m⁻² h⁻¹) [57], and Ag@PDA wooden flower (2.08 kg m⁻² h⁻¹) [58]. Besides, the solar-to-vapor conversion efficiency of Co-CAT evaporator is calculated to be ca. 97.6 %.

The elevated performance of Co-CAT evaporator is supposed to be related to the reduction of water vaporization enthalpy [59–61]. Primarily, the water mass loss using different samples in the darkness is provided (Fig. 7a). The mass loss of pure water (Water) and TC solution (Blank) within 1 h is 252 mg and 249 mg, respectively, which is obviously lower than that using cotton cloth (Cotton, 305 mg), Co-CAT evaporator (Co-CAT, 319 mg), and Co-CAT + PMS (322 mg). As a result, the water vaporization enthalpy using cotton cloth and Co-CAT evaporator is calculated as 2.01 kJ g⁻¹ and 1.92 kJ g⁻¹, respectively

(Note S1), reduced by 17 % and 21 % in comparison to that of water (2.43 kJ g⁻¹). Moreover, to examine the role of Co-CAT in water evaporation enthalpy reduction, poly(vinylidene fluoride) (PVDF) membrane is utilized as the substrate instead of cotton cloth. As shown in Fig. S10, the water mass loss using PVDF membrane (250 mg) is obviously less than that using Co-CAT membrane (296 mg). The corresponding evaporation enthalpy reduces from 2.45 to 2.07 kJ g⁻¹, stating the distinct effect of Co-CAT on the water evaporation enthalpy reduction. Actually, the abundant micropores within Co-CAT promote the formation of water molecular clusters with lower evaporation energy requirement compared with bulk water, owing to the weaker hydrogen-bond interaction with Co-CAT [56]. Meanwhile, cotton cloth can reduce the vaporization enthalpy by forming hydrogen bond between water molecule and hydrophilic cellulose of cotton fibers. Furthermore, DSC measurement was carried out to confirm the adjustment of water molecule state and reduction of evaporation enthalpy by Co-CAT and cotton cloth. As shown in Fig. 7b, the heat flow signals of cotton, Co-CAT evaporator, and Co-CAT powder exhibit broad peaks with gradual decays compared with that of pure water. The evaporation enthalpy based on the DSC result is calculated as 2.41 kJ g⁻¹ (Water), 1.98 kJ g⁻¹ (Cotton), 1.91 kJ g⁻¹ (Co-CAT + Cotton), and 1.40 kJ g⁻¹ (Co-CAT powder), respectively, confirming the positive roles of cotton cloth and Co-CAT in the reduction of water vaporization enthalpy.

COMSOL Multiphysics software (Note S2) was utilized to evaluate the heat management capability of evaporator by simulating the temperature distribution of the evaporation system [62–64]. As depicted in Figs. 7c and 7d, compared with cotton cloth, Co-CAT evaporator exhibits higher surface temperature (329 K vs 315 K) and stronger heat

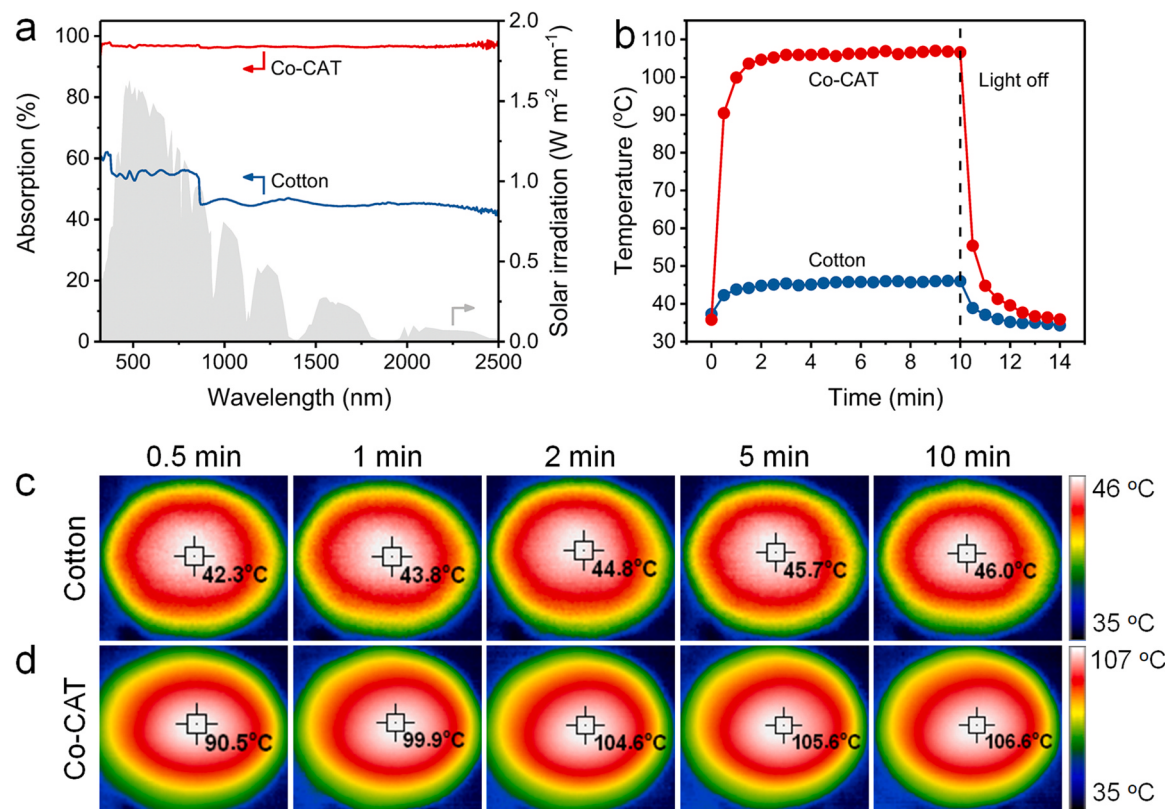


Fig. 5. (a) UV-Vis-NIR absorption spectra, (b) Surface temperature curves, and (c and d) infrared images of cotton cloth and Co-CAT evaporator in dry condition.

localization effect, available for the reduction of heat diffusion into bulk water and the promotion of solar-to-vapor conversion efficiency. Besides, the thermal conductivity of Co-CAT evaporator is barely $0.08 \text{ W m}^{-1} \text{K}^{-1}$, and the heat loss of Co-CAT evaporator is calculated as ca. 19.8 % (Note S3), further verifying the strict thermal management of Co-CAT evaporator.

3.5. AOP catalytic degradation performance of Co-CAT evaporator

The catalytic performance of Co-CAT evaporator for PMS activation was evaluated, and TC was chosen as a model pollutant to be degraded. As shown in Fig. 8a, Co-CAT evaporator presents a negligible adsorption effect of TC, as the relative concentration (C/C_0) of TC solution decreases only 7.4 % in the darkness for static adsorption. Upon exposure to 1 Sun illumination for 60 min, TC is barely degraded (Blank, 6.7 %), and only a small part of TC is eliminated by using Co-CAT evaporator (Co-CAT, 14.2 %). By contrast, a more proportion of TC is removed after adding PMS into TC solution after 60 min (PMS, 65.6 %), illustrating that PMS is effectively activated through sunlight. Notably, the TC degradation efficiency arrives at 67.4 % for 10 min and 91.1 % for 60 min using both Co-CAT evaporator and PMS (Co-CAT + PMS), indicating the obvious catalytic effect of Co-CAT on PMS activation. Supportably, the original HPLC spectra at 60 min are provided in Fig. S11. Moreover, the rate constant (k) is employed to describe the reaction dynamic based on the equation $[\ln(C/C_0) = -kt]$, where C and C_0 refer to the real-time and original concentration of TC, respectively, and t stands for illumination time. As depicted in Fig. 8b, the k of Co-CAT + PMS system (0.063 min^{-1}) distinctly surpasses that of PMS system (0.022 min^{-1}), stating that Co-CAT greatly promotes the reaction rate. The effect of the Co-CAT dosage on the TC degradation performance was studied. As shown in Fig. S12, the evaporator exhibits the poor TC removal performance (6.7 %, 0.0013 min^{-1}), when the Co-CAT dosage is 0 mg. When the Co-CAT dosage is 25, 50 and 75 mg, TC degradation efficiency at 10 min reaches 51.8 %, 67.4 % and 75.7 % respectively.

Meanwhile, k reaches 0.051 , 0.063 and 0.070 min^{-1} respectively, illustrating that the proper increase of Co-CAT dosage is available for the TC degradation. Besides, the influence of the TC and PMS concentrations on the degradation efficiency of TC was investigated. As TC concentration increases from 25 to 100 ppm, the TC degradation efficiency declines from 99.4 % to 63.6 %, and k reduces from 0.231 to 0.024 min^{-1} (Fig. 8c and S13a). When the PMS concentration rises from 0.03 to 0.09 g L^{-1} , the TC elimination efficiency grows from 63.3 % to 96.6 %, and the k increases from 0.03 to 0.108 min^{-1} (Fig. 8d and S13b). In the recyclability test, the TC degradation efficiency keeps around 90 % for 10 cycles (Fig. 8e), demonstrating the good catalytic stability of Co-CAT evaporator.

To investigate the synergy of photothermal conversion and SR-AOPs induced degradation, the influence of illumination on TC degradation was studied (Figs. 8f and S14). As a result, the TC degradation performance using PMS in dark (38.2% , 0.009 min^{-1}) is inferior to that in the sunlight (65.6% , 0.022 min^{-1}), and the degradation performance using Co-CAT + PMS in dark (86.8% , 0.039 min^{-1}) is lower than that in the light (91.1% , 0.063 min^{-1}). The above results declare that illumination not only accelerates the activation of PMS, but also enhances the catalysis of Co-CAT for PMS activation, which can be ascribed to the heat converted from sunlight by Co-CAT to facilitate the PMS activation. In other words, the catalytic degradation of TC is cleverly promoted by the heat localization through the bi-functional Co-CAT. To further prove this inference, we conducted the TC degradation experiment in the existence of PMS and dispersive Co-CAT powder at the bulk temperature of 25°C or 50°C (Fig. S15). As expected, the k at 50°C is up to 0.09 min^{-1} , enhanced by 70 % compared with that at 25°C (0.053 min^{-1}), illustrating that the higher reaction temperature improves the PMS activation to facilitate the catalytic degradation of TC. Supportably, Fig. S16 provides the linear fitting curves of the above-mentioned k .

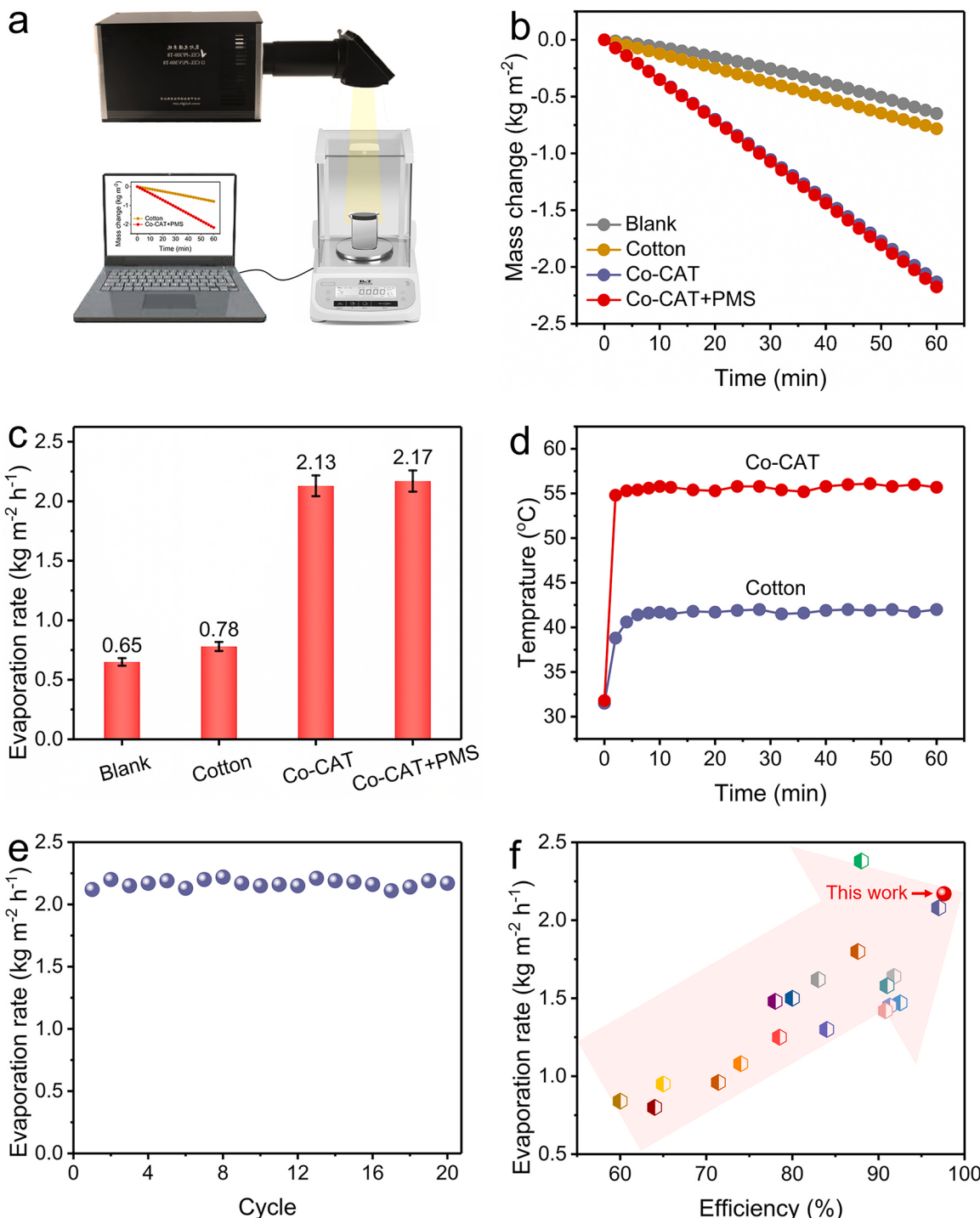


Fig. 6. (a) Scheme of solar steam generation device. (b) Water mass changes and (c) evaporation rates in different conditions: Blank (TC solution under 1 Sun irradiation), Cotton (using cotton cloth), Co-CAT (using Co-CAT evaporator), and Co-CAT + PMS (using Co-CAT evaporator and PMS). (d) Surface temperature curves of Co-CAT evaporator and cotton cloth in wet condition. (e) Recyclability of Co-CAT evaporator. (f) Comparison of the evaporation performance of various solar evaporators.

3.6. TC degradation mechanism using Co-CAT evaporator

Radical quenching experiment was conducted to reveal ROS produced in PMS activation process (Fig. 9a). Various quenching agents were employed to detect the ROS including sulfate radical ($\text{SO}_4^{\bullet-}$), hydroxyl radical ($\cdot\text{OH}$), superoxide radical ($\text{O}_2^{\bullet-}$), and singlet oxygen (${}^1\text{O}_2$). Accordingly, compared with 91.1 % of TC removal in the control group, the degradation efficiency of TC decreases to 84.6 % after adding *tert*-butanol as quencher of $\cdot\text{OH}$, illustrating the existence of $\cdot\text{OH}$. The TC

degradation efficiency reduces to 77.4 % by using ethanol as the quencher of $\text{SO}_4^{\bullet-}$ and $\cdot\text{OH}$, manifesting the existence of both $\text{SO}_4^{\bullet-}$ and $\cdot\text{OH}$. Moreover, the TC removal efficiency sharply declines to 46.3 % after adding *p*-benzoquinone as $\text{O}_2^{\bullet-}$ quencher, implying the significant role of $\text{O}_2^{\bullet-}$ in TC degradation. In addition, the TC removal efficiency reduces to 60.3 % by applying *L*-histidine as ${}^1\text{O}_2$ scavenger, declaring that the non-radical ${}^1\text{O}_2$ is also an essential ROS.

To verify the existence of the above ROS, EPR technology was conducted [37]. DMPO is taken as spin-trapping agent of $\cdot\text{OH}$ and $\text{SO}_4^{\bullet-}$ in

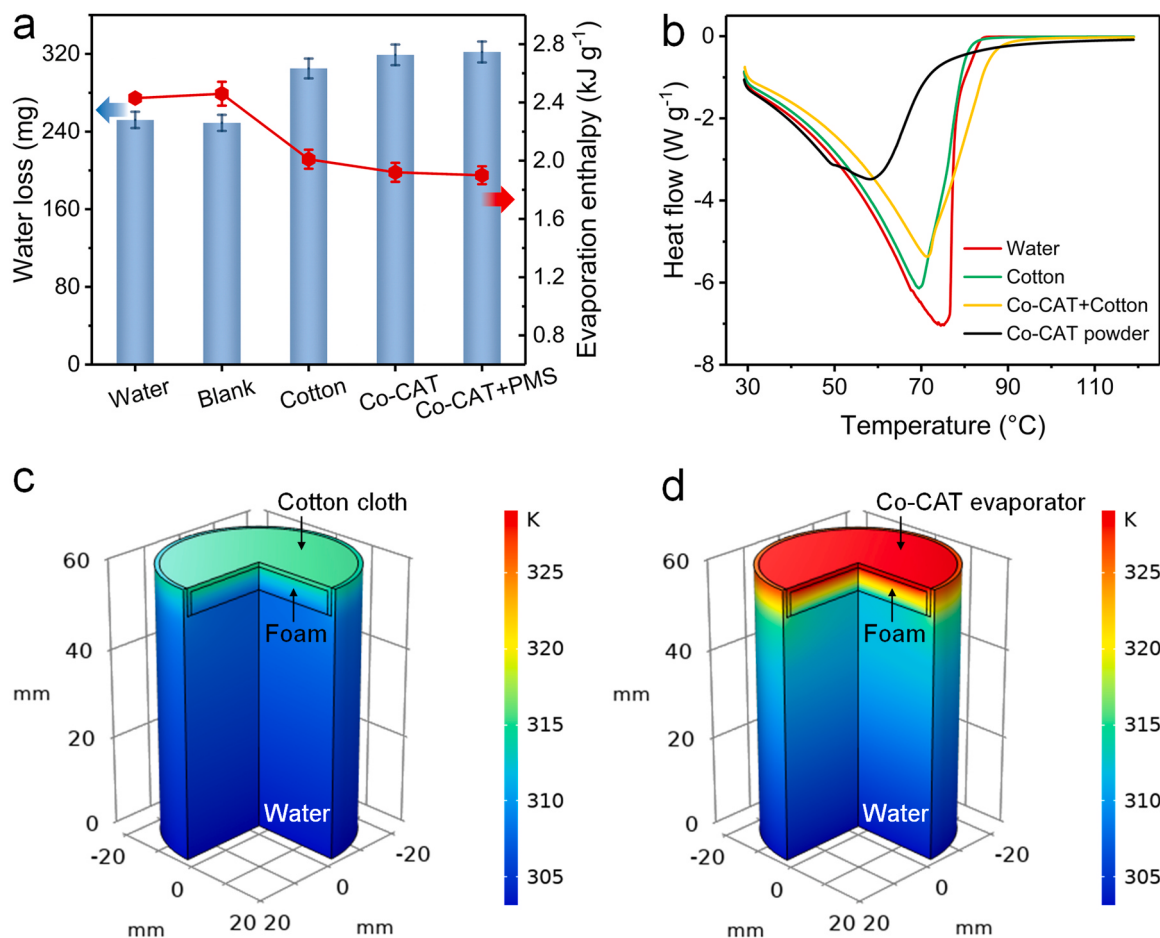
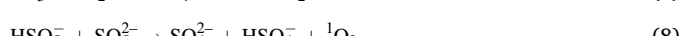


Fig. 7. (a) Water mass loss in the darkness and calculated vaporization enthalpy and (b) DSC curves. COMSOL simulation of (c) cotton cloth and (d) Co-CAT evaporator.

the water medium. As Fig. 9b shows, the four-line signal with the intensity ratio of ca. 1:2:2:1 suggests the presence of ·OH, while the six-line signal confirms the existence of SO₄^{·-}. Besides, DMPO is employed as the trapping agent of O₂^{·-} in ethanol medium, and the corresponding intense six-line signal indicates the generation of O₂^{·-} (Fig. 9c). Furthermore, the triplet signal with the intensity ratio of 1:1:1 manifests the existence of ¹O₂ by using TEMP to trap ¹O₂ in ethanol medium (Fig. 9d). Noticeably, compared with the distinct signals produced in Co-CAT + PMS system, no signals are observed in PMS system (at 0 min), illustrating that the above signals are generated from the PMS decomposition catalyzed by Co-CAT rather than the oxidation of trapping agents. Therefore, it can be inferred that radicals (SO₄^{·-}, ·OH, O₂^{·-}) and nonradical (¹O₂) are involved in Co-CAT + PMS system, which are generated by the variation of cobalt oxidation state (Co²⁺ and Co³⁺) in Co-CAT catalyst. The probable production pathway of ROS is provided in Eqs. (3–8) as follows [65–67],



DFT calculation was performed to simulate the activation of PMS (HSO₅⁻) by Co-CAT [68]. Herein, the (001) crystal plane of Co-CAT is

chosen as the adsorption plane, and Co atom of Co-CAT serves as the active site to interact with O atom of PMS (Fig. 10 A, 10B and S17A). The calculation method is detailed in Note S4. To accurately describe the interaction between PMS and catalyst, the bond length of SO₃O-OH (*l*_{O-O}) and adsorption energy (*E*_{ads}) are calculated. Normally, the free PMS molecule exhibits the *l*_{O-O} of 1.412 Å. After adsorption, the *l*_{O-O} of PMS is stretched to 1.472 Å, which is available for the breakage of O-O bond to produce SO₄^{·-} and other ROS. In addition, the *E*_{ads} of PMS molecule on the Co-CAT is calculated to be -1.201 eV, illustrating that the energy of Co-CAT surface with PMS adsorption is lower than the total energy of exposed Co-CAT surface and isolated PMS, therefore indicating the stability of adsorption. Moreover, difference charge density exhibits that there are the more electron-rich regions in PMS molecule and the more electron-insufficient regions in Co-CAT, illustrating the electron transfer from Co-CAT to PMS (Fig. 10 C, 10D and S17B). The above results confirm the positive role of Co site in Co-CAT for PMS activation. Furthermore, the proposed intermediate products and degradation pathway of TC were identified by UPLC-MS (Fig. S18) [69]. Briefly, TC experiences the de-methylation to form intermediates with the *m/z* value of 433, 418 and 404, which further undergo de-hydroxylation, de-amidization, de-amination and/or ring-opening reaction to generate products with the *m/z* value of 356, 340, 328, 301, 220 and 274. Afterwards, the products are oxidized to smaller molecules with the *m/z* value of 163, 114 and 102, which are finally mineralized to CO₂ and H₂O. According to the TOC analysis, 26.9 % of TC is finally mineralized, suggesting the TC removal with the help of Co-CAT and PMS.

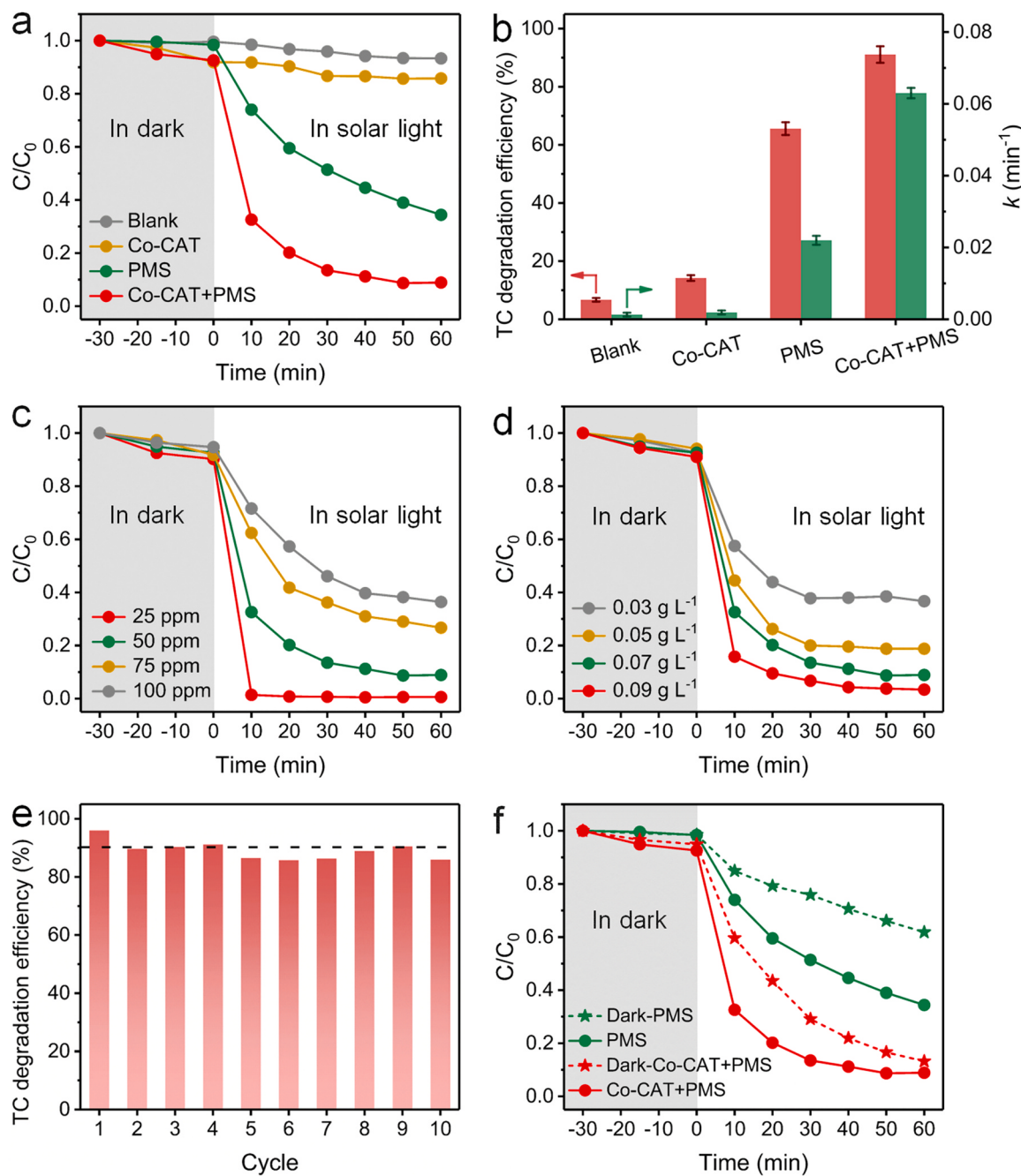


Fig. 8. (a) TC degradation evolution in different conditions and (b) degradation efficiency and k (TC solution: 50 ppm, 75 mL; Co-CAT: 50 mg; PMS: 0.07 g L^{-1}). TC degradation evolution at different concentrations of (c) TC and (d) PMS. (e) Catalytic cycle test of Co-CAT evaporator. (f) TC degradation under controlled illumination.

3.7. Outdoor solar evaporation and TC degradation by Co-CAT evaporator

An outdoor device was constructed to verify the property of Co-CAT evaporator for practical solar evaporation and TC degradation (Figs. 11a and S19). For this device, the evaporator is placed in the container with TC solution (1 L), and the container is placed in the evaporation chamber and supported by the supporting plate (Fig. S20). A nether pipe is used to collect the freshwater sliding from apical condenser, and a upper pipe is utilized to gather the degraded TC solution. As shown in Fig. 11b, a large-sized Co-CAT evaporator (diameter = 16 cm, thickness = 1 cm) is fabricated by coating Co-CAT particles on the surface of cotton cloth supported by foam plate. The device was placed under the

open air of the campus from 8:00–20:00. Initially, there are no droplets formed on the vapor condenser at 8:00 (Figs. 11c and 11e), and droplets are distinctly observed on the vapor condenser within 1 h (Figs. 11d, 11f and 11g). As shown in Fig. 11h, the maximal irradiation intensity and temperature arrive at 0.51 kW m^{-2} and 41.5°C , respectively. Accordingly, the highest water production rate by using the self-designed device is $0.58 \text{ kg m}^{-2} \text{ h}^{-1}$, and the total water production within 12 h reaches 4.05 kg m^{-2} (Fig. 11i). Hereby, the water production by a 1 m^2 device (4.05 kg) is sufficient for the basic water requirement of an adult per day (2.5 L) [70].

It should be noted that the reduced evaporation rate in the outdoor solar evaporation is due to the lower irradiation intensity, compared to that of the indoor solar evaporation. Evidently, the development of solar

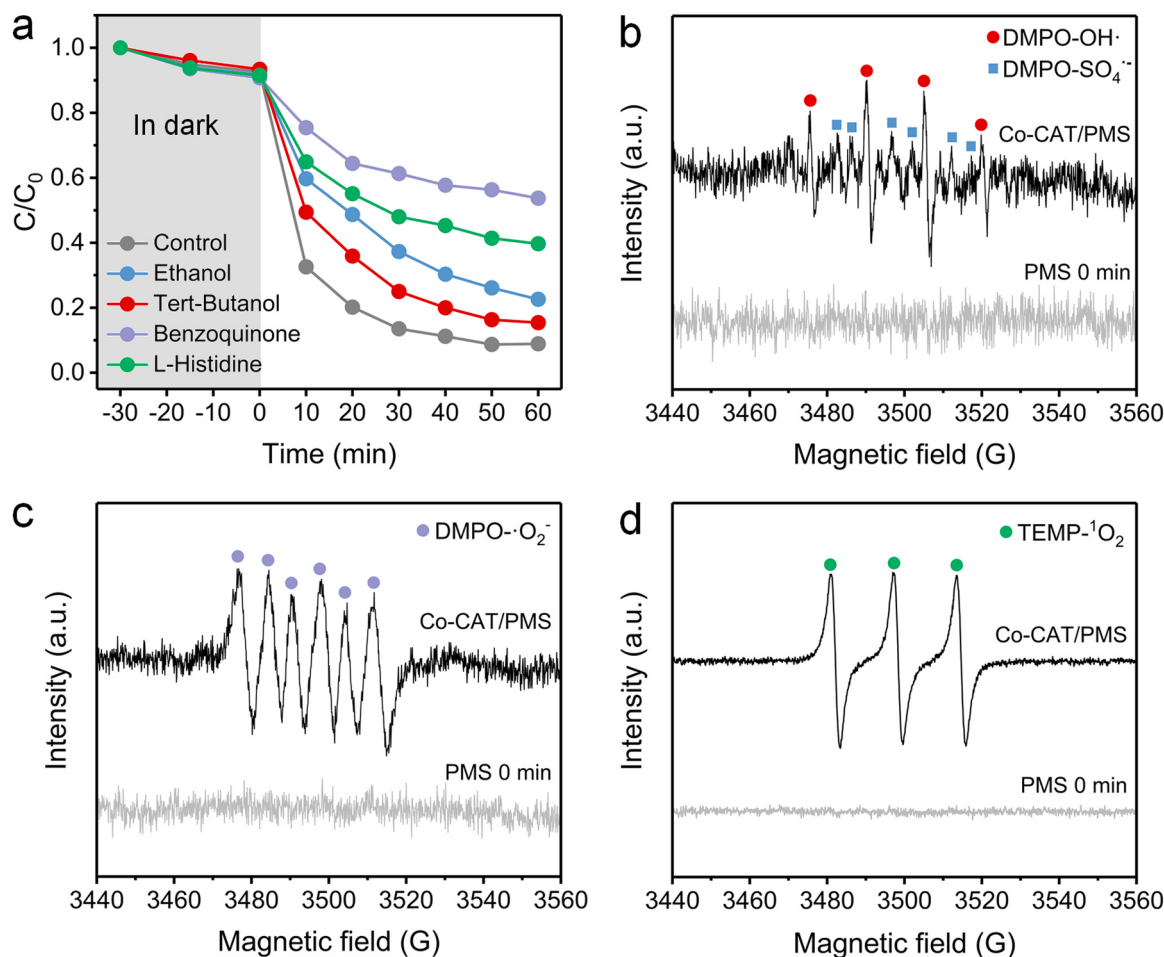


Fig. 9. (a) TC degradation evolution by using radical quenchers, therein [Ethanol] = [tert-Butanol] = 0.2 M, and [*p*-Benzoquinone] = [*L*-Histidine] = 0.005 M. (b-d) EPR spectra by using radical trapping agents, therein [PMS] = 0.07 g L⁻¹ (0.2 mM), [Co-CAT] = 1 g L⁻¹, [DMPO] = 0.4 M, and [TEMP] = 0.3 M.

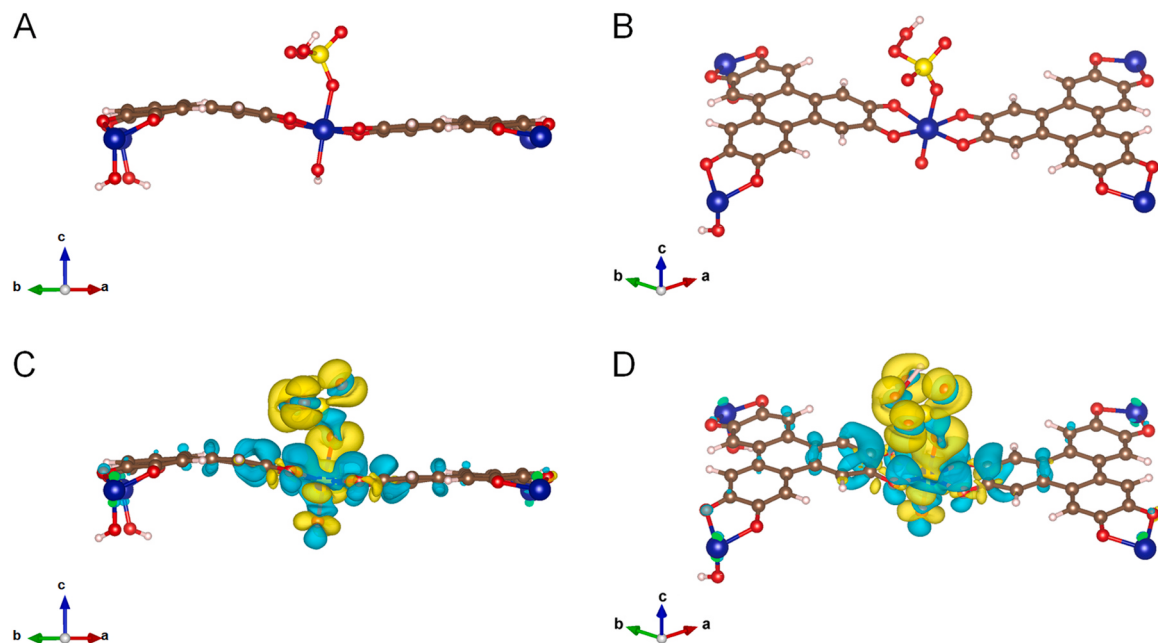


Fig. 10. (A and B) DFT adsorption models of PMS molecule on the (001) crystal face of Co-CAT. (C and D) Schemes of difference charge density for PMS adsorbed on Co-CAT. The green areas stand for electron-insufficient region, and yellow areas stand for electron-rich region. Color code: O, red; S, yellow; Co, blue; C, brown; H, white.

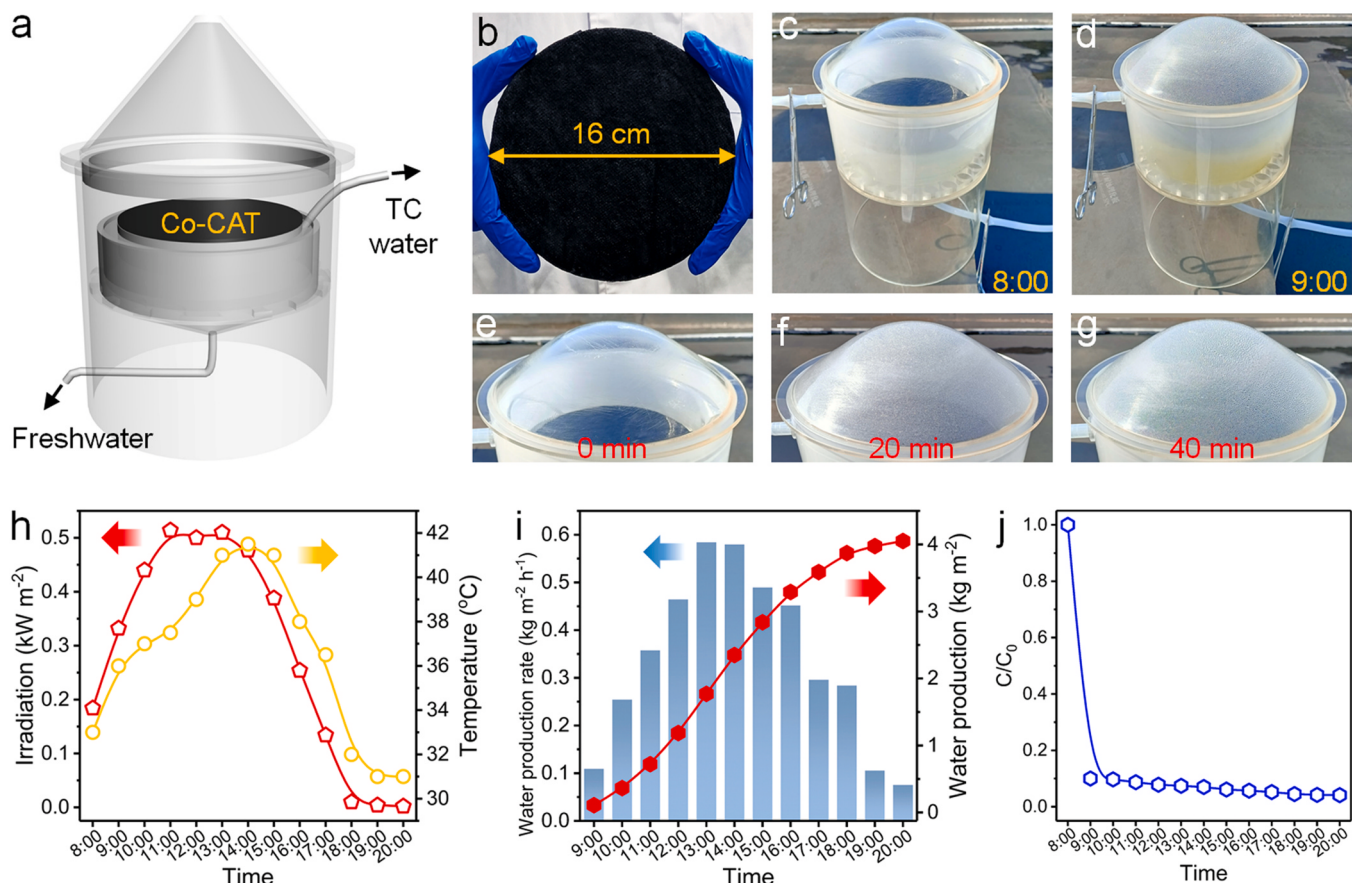


Fig. 11. (a) Scheme of outdoor device made from poly(methyl methacrylate). Photographs of (b) Co-CAT evaporator, (c and d) outdoor device at 8:00 and 9:00, and (e–g) water evaporation progress within 40 min. (h) Evolution of illumination intensity and temperature. (i) Water evaporation rate and cumulative production evolution. (j) TC removal evolution.

evaporation systems capable of high light absorption and accelerated condensation of water droplets is highly needed to improve the practical freshwater production. Additionally, as shown in Fig. 11j, the TC removal efficiency reaches 90.0 % after 1 h and 95.9 % after 12 h, illustrating the good catalytic property of Co-CAT evaporator. Supporably, Fig. S21 displays the progress of TC degradation and water evaporation throughout the day. The above results demonstrate the potential application of Co-CAT evaporator in freshwater production and water purification.

4. Conclusion

In summary, we have prepared a dual-functional evaporator by dip-coating Co-CAT particles on cotton cloth for interfacial evaporation and TC degradation. Co-CAT is endowed with “all-in-one” features, i.e., superior light absorption, abundant pore structures, and high AOP catalytic activity. The large specific surface area ($418 \text{ m}^2 \text{ g}^{-1}$) and abundant micropore (1.4 nm) of Co-CAT are available for the transport of water and the reduction of water evaporation enthalpy. The uniformly distributed Co sites within Co-CAT serve as catalytic center to decompose PMS into ROS including SO_4^{2-} , $\cdot\text{OH}$, O_2^- and ${}^1\text{O}_2$, which further oxidized TC to achieve the contaminant degradation. Moreover, cotton cloth composed of hydrophilic cellulose ensures fast water transport. Consequently, the bi-functional Co-CAT evaporator exhibits rapid water evaporation ($2.2 \text{ kg m}^{-2} \text{ h}^{-1}$) and efficient TC degradation (91.1 %) by PMS activation under 1 Sun irradiation, and displays the synergy of photothermal evaporation and AOP-induced catalytic degradation. This work offers a novel way to realize the well-integrated combination of freshwater production and sewage purification. Notably, more effort

should be made on the development of new advanced solar evaporators capable of high light absorption and good catalytic activity for achieving higher mineralization efficiency in the future work.

CRediT authorship contribution statement

Panpan He: Methodology, Data curation, Formal analysis, Writing & editing. Hongyu Lan: Methodology, Data curation, Formal analysis. Huiying Bai: Methodology, Data curation, Formal analysis. Yingying Zhu: Methodology, Data curation, Formal analysis. Zifan Fan: Methodology, Investigation, Data curation. Jie Liu: Methodology, Data curation. Lijie Liu: Methodology, Data curation. Ran Niu: Methodology, Data curation, Formal analysis. Zhiyue Dong: Writing – review & editing, Supervision, Funding acquisition. Jiang Gong: Project administration, Writing – review & editing, Supervision, Funding acquisition.

Declaration of Competing Interest

The authors declare that they have no known competing financial interests or personal relationships that could have appeared to influence the work reported in this paper.

Data availability

Data will be made available on request.

Acknowledgements

The present work is supported by National Natural Science

Foundation of China (No. 51903099 and 22101077), the Youth Foundation of Hubei Province (No. 2021CFB092), 100 Talents Program of Hubei Provincial Government, Huazhong University of Science and Technology (No. 3004013134), the Innovation and Talent Recruitment Base of New Energy Chemistry and Device (No. B21003), the “Chu-Tian Scholar” Program of Hubei Province, the Open Research Fund (No. 2022JYBF01) of Key Laboratory of Material Chemistry for Energy Conversion and Storage (HUST), Ministry of Education, and the Opening Project (No. KFKT2304) of the Key Laboratory of Polymer Processing Engineering (South China University of Technology), Ministry of Education. We are grateful to the Analytical and Testing Centre of HUST for access to their facilities.

Appendix A. Supporting information

Supplementary data associated with this article can be found in the online version at doi:10.1016/j.apcatb.2023.123001.

References

- [1] F. Li, N. Li, S. Wang, L. Qiao, L. Yu, P. Murto, X. Xu, Self-repairing and damage-tolerant hydrogels for efficient solar-powered water purification and desalination, *Adv. Funct. Mater.* 31 (2021), 2104464.
- [2] P. Tao, G. Ni, C. Song, W. Shang, J. Wu, J. Zhu, G. Chen, T. Deng, Solar-driven interfacial evaporation, *Nat. Energy* 3 (2018) 1031–1041.
- [3] L. Zhou, X. Li, G.W. Ni, S. Zhu, J. Zhu, The revival of thermal utilization from the Sun: interfacial solar vapor generation, *Nat. Sci. Rev.* 6 (2019) 562–578.
- [4] X. Wu, Z. Wu, Y. Wang, T. Gao, Q. Li, H. Xu, All-cold evaporation under One Sun with zero energy loss by using a heatsink inspired solar evaporator, *Adv. Sci.* 8 (2021), 202002501.
- [5] S.L. Wu, H. Chen, H.L. Wang, X. Chen, H.C. Yang, S.B. Darling, Solar-driven evaporators for water treatment: challenges and opportunities, *Environ. Sci. Water Res. Technol.* 7 (2021) 24–39.
- [6] B. Zhang, P.W. Wong, A.K. An, Photothermally enabled MXene hydrogel membrane with integrated solar-driven evaporation and photodegradation for efficient water purification, *Chem. Eng. J.* 430 (2022), 133054.
- [7] N. Liu, L. Hao, B. Zhang, R. Niu, J. Gong, T. Tang, Rational design of high-performance bilayer solar evaporator by using waste polyester-derived porous carbon-coated wood, *Energy Environ. Mater.* 5 (2022) 617–626.
- [8] L. Zhu, T. Ding, M. Gao, C.K.N. Peh, G.W. Ho, Shape conformal and thermal insulative organic solar absorber sponge for photothermal water evaporation and thermoelectric power generation, *Adv. Energy Mater.* 9 (2019), 1900250.
- [9] Y. Kuang, C. Chen, S. He, E.M. Hitz, Y. Wang, W. Gan, R. Mi, L. Hu, A high-performance self-regenerating solar evaporator for continuous water desalination, *Adv. Mater.* 31 (2019), 1900498.
- [10] X. Mu, J. Zhou, P. Wang, H. Chen, T. Yang, S. Chen, L. Miao, T. Mori, A robust starch-polyacrylamide hydrogel with scavenging energy harvesting capacity for efficient solar thermoelectricity-freshwater cogeneration, *Energy Environ. Sci.* 15 (2022) 3388–3399.
- [11] W. Wang, Y. Shi, C. Zhang, S. Hong, L. Shi, J. Chang, R. Li, Y. Jin, C. Ong, S. Zhuo, P. Wang, Simultaneous production of fresh water and electricity via multistage solar photovoltaic membrane distillation, *Nat. Commun.* 10 (2019) 3012.
- [12] T. Zhang, F. Meng, M. Gao, W.L. Ong, K.-G. Haw, T. Ding, G.W. Ho, S. Kawi, Multi-interfacial catalyst with spatially defined redox reactions for enhanced pure water photothermal hydrogen production, *EcoMat* 3 (2021), e12152.
- [13] Y. Wang, X. Wu, T. Gao, Y. Lu, X. Yang, G.Y. Chen, G. Owens, H. Xu, Same materials, bigger output: a reversibly transformable 2D–3D photothermal evaporator for highly efficient solar steam generation, *Nano Energy* 79 (2021), 105477.
- [14] L. Li, J. Zhang, Highly salt-resistant and all-weather solar-driven interfacial evaporators with photothermal and electrothermal effects based on janus graphene@silicone sponges, *Nano Energy* 81 (2021), 105682.
- [15] X. Zhou, Y. Guo, F. Zhao, W. Shi, G. Yu, Topology-controlled hydration of polymer network in hydrogels for solar-driven wastewater treatment, *Adv. Mater.* 32 (2020), 2007012.
- [16] F. Zhao, Y. Guo, X. Zhou, W. Shi, G. Yu, Materials for solar-powered water evaporation, *Nat. Rev. Mater.* 5 (2020) 388–401.
- [17] K. Xu, C. Wang, Z. Li, S. Wu, J. Wang, Salt mitigation strategies of solar-driven interfacial desalination, *Adv. Funct. Mater.* 31 (2021), 2007855.
- [18] Y. Wang, X. Wu, T. Gao, Y. Lu, X. Yang, G.Y. Chen, G. Owens, H. Xu, Same materials, bigger output: a reversibly transformable 2D–3D photothermal evaporator for highly efficient solar steam generation, *Nano Energy* 79 (2021), 105477.
- [19] T. Ding, Y. Zhou, W.L. Ong, G.W. Ho, Hybrid solar-driven interfacial evaporation systems: beyond water production towards high solar energy utilization, *Mater. Today* 42 (2021) 178–191.
- [20] T. Ding, G.W. Ho, Using the sun to co-generate electricity and freshwater, *Joule* 5 (2021) 1639–1641.
- [21] F.L. Meng, M. Gao, T. Ding, G. Yilmaz, W.L. Ong, G.W. Ho, Modular deformable steam electricity cogeneration system with photothermal, water, and electrochemical tunable multilayers, *Adv. Funct. Mater.* 30 (2020), 2002867.
- [22] H. Wang, C. Zhang, Z. Zhang, B. Zhou, J. Shen, A. Du, Artificial trees inspired by monstera for highly efficient solar steam generation in both normal and weak light environments, *Adv. Funct. Mater.* 30 (2020), 2005513.
- [23] M. Gao, T. Zhang, G.W. Ho, Advances of photothermal chemistry in photocatalysis, thermocatalysis, and synergistic photothermocatalysis for solar-to-fuel generation, *Nano Res.* 15 (2022) 9985–10005.
- [24] R. Djellabi, L. Noureen, V.-D. Dao, D. Meroni, E. Falletta, D.D. Dionysiou, C. L. Bianchi, Recent advances and challenges of emerging solar-driven steam and the contribution of photocatalytic effect, *Chem. Eng. J.* 431 (2022), 134024.
- [25] S. Yan, H. Song, Y. Li, J. Yang, X. Jia, S. Wang, X. Yang, Integrated reduced graphene oxide/polypyrrole hybrid aerogels for simultaneous photocatalytic decontamination and water evaporation, *Appl. Catal. B Environ.* 301 (2022), 120820.
- [26] D. Xie, M. He, X. Li, J. Sun, J. Luo, Y. Wu, F. Cheng, Tree-inspired efficient solar evaporation and simultaneous in-situ purification of ultra-highly concentrated mixed volatile organic wastewater, *Nano Energy* 93 (2022), 106802.
- [27] B. Chen, X. Zhang, Y. Xia, G. Liu, H. Sang, Y. Liu, J. Yuan, J. Liu, C. Ma, Y. Liang, M. Song, G. Jiang, Harnessing synchronous photothermal and photocatalytic effects of cryptomelane-type MnO₂ nanowires towards clean water production, *J. Mater. Chem. A* 9 (2021) 2414–2420.
- [28] X. Duan, H. Sun, S. Wang, Metal-free carbocatalysis in advanced oxidation reactions, *Acc. Chem. Res.* 51 (2018) 678–687.
- [29] J. Lin, W. Tian, Z. Guan, H. Zhang, X. Duan, H. Wang, H. Sun, Y. Fang, Y. Huang, S. Wang, Functional carbon nitride materials in photo-fenton-like catalysis for environmental remediation, *Adv. Funct. Mater.* 32 (2022), 2201743.
- [30] Y. Shang, X. Xu, B. Gao, S. Wang, X. Duan, Single-atom catalysis in advanced oxidation processes for environmental remediation, *Chem. Soc. Rev.* 50 (2021) 5281–5322.
- [31] Y. Li, H. Zhang, D. Fan, Z. Chen, X. Yang, Coupling solar-driven photothermal effect into photocatalysis for sustainable water treatment, *J. Hazard. Mater.* 423 (2022), 127128.
- [32] C. Chen, T. Ma, Y. Shang, B. Gao, B. Jin, H. Dan, Q. Li, Q. Yue, Y. Li, Y. Wang, X. Xu, In-situ pyrolysis of enteromorpha as carbocatalyst for catalytic removal of organic contaminants: considering the intrinsic N/Fe in enteromorpha and non-radical reaction, *Appl. Catal. B Environ.* 250 (2019) 382–395.
- [33] S. Giannakis, K.Y.A. Lin, F. Ghanbari, A review of the recent advances on the treatment of industrial wastewaters by sulfate radical-based advanced oxidation processes (SR-AOPs), *Chem. Eng. J.* 406 (2021), 127083.
- [34] Y. Wang, S. Hui, S. Zhan, R. Djellabi, J. Li, X. Zhao, Activation of peroxyomonosulfate by novel Pt/Al₂O₃ membranes via a nonradical mechanism for efficient degradation of electron-rich aromatic pollutants, *Chem. Eng. J.* 381 (2020), 122563.
- [35] W.D. Oh, Z. Dong, T.T. Lim, Generation of sulfate radical through heterogeneous catalysis for organic contaminants removal: current development, challenges and prospects, *Appl. Catal. B Environ.* 194 (2016) 169–201.
- [36] R. Zhou, H. Song, D. Zu, S. Pan, Y. Wang, F. Wang, Z. Li, Y. Shen, C. Li, Self-floating Ti₃C₂ MXene-coated polyurethane sponge with excellent photothermal conversion performance for peroxydisulfate activation and clean water production, *Sep. Purif. Technol.* 282 (2022), 119990.
- [37] H. Bai, P. He, L. Hao, Z. Fan, R. Niu, T. Tang, J. Gong, Waste-treating-waste: upcycling discarded polyester into metal–organic framework nanorod for synergistic interfacial solar evaporation and sulfate-based advanced oxidation process, *Chem. Eng. J.* 456 (2023), 140994.
- [38] X. Yin, Y. Zhang, X. Xu, Y. Wang, Bilayer fiber membrane electrospun from MOF derived Co₃S₄ and PAN for solar steam generation induced sea water desalination, *J. Solid State Chem.* 303 (2021), 122423.
- [39] Z. Xiong, Y. Jiang, Z. Wu, G. Yao, B. Lai, Synthesis strategies and emerging mechanisms of metal–organic frameworks for sulfate radical-based advanced oxidation process: a review, *Chem. Eng. J.* 421 (2021), 127863.
- [40] M. Hao, M. Qiu, H. Yang, B. Hu, X. Wang, Recent advances on preparation and environmental applications of MOF-derived carbons in catalysis, *Sci. Total Environ.* 760 (2021), 143333.
- [41] X. Gui, K. Chen, H. Xing, Q. Yang, R. Krishna, Z. Bao, H. Wu, W. Zhou, X. Dong, Y. Han, B. Li, Q. Ren, M.J. Zawortkotko, B. Chen, Pore chemistry and size control in hybrid porous materials for acetylene capture from ethylene, *Science* 353 (2016) 141–144.
- [42] Q. Wang, D. Astruc, State of the art and prospects in metal–organic framework (MOF)-based and MOF-derived nanocatalysis, *Chem. Rev.* 120 (2020) 1438–1511.
- [43] W. Fan, X. Zhang, Z. Kang, X. Liu, D. Sun, Isoreticular chemistry within metal–organic frameworks for gas storage and separation, *Coord. Chem. Rev.* 443 (2021), 213968.
- [44] W.P. Lustig, S. Mukherjee, N.D. Rudd, A.V. Desai, J. Li, S.K. Ghosh, Metal–organic frameworks: functional luminescent and photonic materials for sensing applications, *Chem. Soc. Rev.* 46 (2017) 3242–3285.
- [45] X. Xiao, L. Zou, H. Pang, Q. Xu, Synthesis of micro/nanoscaled metal–organic frameworks and their direct electrochemical applications, *Chem. Soc. Rev.* 49 (2020) 301–331.
- [46] H. Wang, C. Zhang, X. Ji, J. Yang, Z. Zhang, Y. Ma, Z. Zhang, B. Zhou, J. Shen, A. Du, Over 11 kg m⁻² h⁻¹ evaporation rate achieved by cooling metal–organic framework foam with pine needle-like hierarchical structures to subambient temperature, *ACS Appl. Mater. Interfaces* 14 (2022) 10257–10266.
- [47] Y. Song, N. Xu, G. Liu, H. Qi, W. Zhao, B. Zhu, L. Zhou, J. Zhu, High-yield solar-driven atmospheric water harvesting of metal–organic-framework-derived

- nanoporous carbon with fast-diffusion water channels, *Nat. Nanotechnol.* 17 (2022) 857–863.
- [48] C. Wang, J. Kim, V. Malgras, J. Na, J. Lin, J. You, M. Zhang, J. Li, Y. Yamauchi, Metal-organic frameworks and their derived materials: emerging catalysts for a sulfate radicals-based advanced oxidation process in water purification, *Small* 15 (2019), 1900744.
- [49] M. Hmadedeh, Z. Lu, Z. Liu, F. Gándara, H. Furukawa, S. Wan, V. Augustyn, R. Chang, L. Liao, F. Zhou, E. Perre, V. Ozolins, K. Suenaga, X. Duan, B. Dunn, Y. Yamamoto, O. Terasaki, O.M. Yaghi, New porous crystals of extended metal-catecholates, *Chem. Mater.* 24 (2012) 3511–3513.
- [50] Z. Dong, C. Zhang, H. Peng, J. Gong, Q. Zhao, Modular design of solar-thermal nanofluidics for advanced desalination membranes, *J. Mater. Chem. A* 8 (2020) 24493–24500.
- [51] S. Wang, Y. Niu, C. Wang, F. Wang, Z. Zhu, H. Sun, W. Liang, A. Li, Modified hollow glass microspheres/reduced graphene oxide composite aerogels with low thermal conductivity for highly efficient solar steam generation, *ACS Appl. Mater. Interfaces* 13 (2021) 42803–42812.
- [52] K. Chen, L. Li, J. Zhang, Design of a separated solar interfacial evaporation system for simultaneous water and salt collection, *ACS Appl. Mater. Interfaces* 13 (2021) 59518–59526.
- [53] J. Ren, Y. Ding, J. Gong, J. Qu, R. Niu, Simultaneous solar-driven steam and electricity generation by cost-effective, easy scale-up MnO₂-based flexible membranes, *Energy Environ. Mater.* 6 (2023), e12376.
- [54] H. Bai, N. Liu, L. Hao, P. He, C. Ma, R. Niu, J. Gong, T. Tang, Self-floating efficient solar steam generators constructed using super-hydrophilic N,O dual-doped carbon foams from waste polyester, *Energy Environ. Mater.* 5 (2022) 1204–1213.
- [55] D. Xu, C. Ge, Z. Chen, Y. Liu, H. Du, H. Gong, C. Gao, Z. Shen, W. Xu, K. Liu, Composite braided fabric coupled with photothermal and electrothermal processes for stable and continuous all-day desalination, *ACS Appl. Mater. Interfaces* 14 (2022) 52087–52095.
- [56] X. Chen, C. Meng, Y. Wang, Q. Zhao, Y. Li, X.M. Chen, D. Yang, Y. Li, Y. Zhou, Laser-synthesized rutile TiO₂ with abundant oxygen vacancies for enhanced solar water evaporation, *ACS Sustain. Chem. Eng.* 8 (2020) 1095–1101.
- [57] K. Kim, S. Yu, C. An, S.W. Kim, J.H. Jang, Mesoporous three-dimensional graphene networks for highly efficient solar desalination under 1 Sun illumination, *ACS Appl. Mater. Interfaces* 10 (2018) 15602–15608.
- [58] S. Chen, Z. Sun, W. Xiang, C. Shen, Z. Wang, X. Jia, J. Sun, C.J. Liu, Plasmonic wooden flower for highly efficient solar vapor generation, *Nano Energy* 76 (2020), 104998.
- [59] B. Chen, J. Ren, Y. Song, P. He, H. Bai, Z. Fan, R. Niu, J. Gong, Upcycling waste poly(ethylene terephthalate) into a porous carbon cuboid through a MOF-derived carbonization strategy for interfacial solar-driven water-thermoelectricity cogeneration, *ACS Sustain. Chem. Eng.* 10 (2022) 16427–16439.
- [60] F. Zhao, X. Zhou, Y. Shi, X. Qian, M. Alexander, X. Zhao, S. Mendez, R. Yang, L. Qu, G. Yu, Highly efficient solar vapour generation via hierarchically nanostructured gels, *Nat. Nanotechnol.* 13 (2018) 489–495.
- [61] H. Yao, P. Zhang, C. Yang, Q. Liao, X. Hao, Y. Huang, M. Zhang, X. Wang, T. Lin, H. Cheng, J. Yuan, L. Qu, Janus-interface engineering boosting solar steam towards high-efficiency water collection, *Energy Environ. Sci.* 14 (2021) 5330–5338.
- [62] R. Niu, Y. Ding, L. Hao, J. Ren, J. Gong, J. Qu, Plant-mimetic vertical-channel hydrogels for synergistic water purification and interfacial water evaporation, *ACS Appl. Mater. Interfaces* 14 (2022) 45533–45544.
- [63] Z. Fan, J. Ren, H. Bai, P. He, L. Hao, N. Liu, B. Chen, R. Niu, J. Gong, Shape-controlled fabrication of MnO/C hybrid nanoparticle from waste polyester for solar evaporation and thermoelectricity generation, *Chem. Eng. J.* 451 (2023), 138534.
- [64] L. Chen, J. Ren, J. Gong, J. Qu, R. Niu, Cost-effective, scalable fabrication of self-floating xerogel foam for simultaneous photothermal water evaporation and thermoelectric power generation, *Chem. Eng. J.* 454 (2023), 140383.
- [65] Y. Wang, X. Li, X. Hu, Z. Su, A novel 3D cobalt(II) metal-organic framework to activate peroxymonosulfate for degradation of organic dyes in water, *J. Solid State Chem.* 289 (2020), 121443.
- [66] H. Fu, S. Ma, P. Zhao, S. Xu, S. Zhan, Activation of peroxymonosulfate by graphitized hierarchical porous biochar and MnFe₂O₄ magnetic nanoarchitecture for organic pollutants degradation: structure dependence and mechanism, *Chem. Eng. J.* 360 (2019) 157–170.
- [67] K. Wang, C. Han, F. Li, Y. Liu, Z. Shao, L. Liu, S. Wang, S. Liu, An intrinsic descriptor of perovskite cobalts for catalytic peroxymonosulfate activation toward water remediation, *Appl. Catal. B Environ.* 320 (2023), 121990.
- [68] J. Wei, D. Han, J. Bi, J. Gong, Fe-doped ilmenite CoTiO₃ for antibiotic removal: electronic modulation and enhanced activation of peroxymonosulfate, *Chem. Eng. J.* 423 (2021), 130165.
- [69] S. Zhang, H. Gao, X. Xu, R. Cao, H. Yang, X. Xu, J. Li, MOF-derived CoN/N-C@SiO₂ yolk-shell nanoreactor with dual active sites for highly efficient catalytic advanced oxidation processes, *Chem. Eng. J.* 381 (2020), 122670.
- [70] Y. Wang, X. Wu, B. Shao, X. Yang, G. Owens, H. Xu, Boosting solar steam generation by structure enhanced energy management, *Sci. Bull.* 65 (2020) 1380–1388.